Diurnal Variability of Regional Cloud and Clear-Sky Radiative Parameters Derived from GOES Data. Part I: Analysis Method

PATRICK MINNIS AND EDWIN F. HARRISON

Atmospheric Sciences Division, NASA Langley Research Center, Hampton, VA 23665

(Manuscript received 8 November 1982, in final form 27 April 1984)

ABSTRACT

A hybrid bispectral threshold method (HBTM) is developed for hourly regional cloud and radiative parameters from geostationary satellite visible and infrared radiance data. The quantities derived with the HBTM include equivalent blackbody temperatures for clear skies, for the total cloud cover and for the cloud cover at three levels in the atmosphere; the total fractional cloud cover and the fractional cloud amounts at three altitudes; and the clear-sky and total cloud reflectance characteristics. Geostationary satellite data taken during November 1978 are analyzed. A minimum reflectance technique is used to determine clear-sky brightness. A visible bidirectional reflectance model is derived for clear ocean areas. Clear-sky radiative temperature is found with a bispectral clear radiance technique during daylight hours. An empirical model is derived to predict clear-sky temperature at night. A combination of previously published infrared threshold and bispectral techniques is used to determine the remaining parameters. Sources of uncertainty are discussed and means to minimize them are proposed. Monthly mean, regional fractional cloudiness determined with this method agrees well with more conventional subjective techniques. On the average, the present results are approximately 0.05 less than corresponding surface observations; this is consistent with previous comparisons of satellite- and surface-based nephanalyses. Comparisons between subjective analyses of satellite photographs and the HBTM yielded average differences in mean regional cloudiness, mean hourly cloudiness and instantaneous cloud amounts of 0.04, 0.05 and 0.11 respectively. Root-mean-square differences in these same quantities derived by two satellite data analysts were 0.03, 0.04 and 0.08 respectively.

1. Introduction

The accuracy of Earth radiation budget (ERB) estimates derived from satellite-based measurements is highly dependent on how well cloud variability is taken into account. Because of its dynamic nature and pronounced optical characteristics, cloud cover is one of the most important variables affecting the radiation balance and, ultimately, the global climate. Recent ERB measurements (Raschke *et al.*, 1973; Vonder Haar *et al.*, 1981) have been taken from satellites in sun-synchronous orbits. This type of orbit limits observations of a given nonpolar area to only two local times, 12 hours apart at the equator. In the analyses of the above ERB data sets, it was necessary, because of the sampling limitations, to implicitly assume that the average monthly cloudiness in a given region is independent of the time of day. Thus, radiation budgets computed for regions having systematic diurnal changes in cloud distribution or cloud optical characteristics may contain substantial bias errors. It is well-known that diurnal cloud cycles occur in many areas (Sherr *et al.*, 1968; Short and Wallace, 1980), but the magnitude and timing of these daily cloud oscillations and their radiative properties are poorly known.

Cloud cover has been observed from space since the launch of the first weather satellite (Arking, 1964; Clapp, 1964; Miller and Feddes, 1971; Sadler *et al.*, 1976). Most satellite nephanalyses have provided a global view of seasonal cloud patterns and weather systems, but their applicability to ERB calculations is limited by the subjectivity in most of the analysis procedures, by sampling constraints, and by a lack of definitive data about the radiative properties of the cloud cover. Sherr *et al.* (1968) developed a global cloud-cover model from ground- and satellite-based observations. Although their model has global coverage and diurnal resolution, they provide no information about the cloud radiative properties, and they assume that data from a single station are representative of a much larger ($>10^4$ km^2) region of climatological homogeneity. More recently, Bean and Somerville (1981) developed a global cloud model from Tiros satellite measurements, but diurnal variability and radiative properties were not included. A more comprehensive description of cloud cover was constructed by Cox and Griffith (1979b) from a combination of radar and satellite observations for use in radiative divergence calculations. Their data, though, were limited to the A/B array and Phase III of the GARP Atlantic Tropical Experiment (GATE).

The radiative properties of isolated clouds have been researched extensively with various models (Dave and Braslau, 1975; McKee and Klehr, 1978; Davis *et al.*, 1979). The reflectance properties of certain cloud combinations have also been examined in an analog experiment (Kuenning *et al.*, 1978). Cloud modeling efforts have been effective in demonstrating the complexities of cloud radiative interactions and in the development of cloud radiative parameterizations (Liou and Wittman, 1979). In addition, aircraft observations have provided some empirical data for the shortwave (e.g., Griggs, 1968) and longwave properties (e.g., Herman, 1980) of certain cloud types. However, observations and comprehensive models of the radiative effects of time-varying, extended cloudiness are scarce.

Conflicting reports on the effects of cloud-albedo feedback (Paltridge, 1980) are also indicative of the dearth of information on the distribution of clouds and their radiative properties. Without more comprehensive observations of cloudiness and its properties, it will not be possible to accurately account for the radiative influence of clouds in climate models (Hansen *et al.*, 1981).

This paper examines several aspects of the effects of extended cloudiness using hourly visible and infrared data from the Geostationary Operational Environmental Satellite (GOES). A methodology called the hybrid bispectral threshold method is developed in Part I to extract regional cloud amounts at three levels in the atmosphere, effective cloud-top temperatures, clear-sky temperature and cloud and clear-sky visible reflectance characteristics from GOES data. Part II examines the diurnal variations in low, middle, high and total cloudiness determined with this methodology for November 1978. In Part III, the bulk, broadband radiative properties of the resultant cloud and clear-sky data are estimated to determine how the diurnal variability of regional cloudiness might influence the interpretation of ERB measurements.

2. Data

This analysis utilizes hourly digital data from the GOES-2 Visible and Infrared Spin Scan Radiometer (VISSR) for November 1978. GOES-2 (East) was located over 0° latitude and 75°W longitude. Infrared (unispectral) data were obtained between 0000 and 1100 GMT, while colocated visible and infrared (bispectral) counts were saved between 1200 and 2300 GMT.

Measurements in the infrared (IR) window (10.5–12.5 μm) were taken at a nominal sub-satellite resolution of 8 km and stored as counts ranging from 0 to 255. Equivalent blackbody temperature T^* is found for each IR count from a calibrated look-up table. This temperature is closely related to the radiative temperature of the underlying surface. A simple model is given below only to illustrate the relationship between T^* and the temperature of the underlying background, T_b. The background may be either a terrestrial surface or a cloud surface, or a combination of the two:

$$T^* = TBB[\epsilon_b BB(T_b)\tau_A + (1 - \tau_A)BB(T_A)], \quad (1)$$

where ϵ_b is the background emissivity, τ_A the effective transmittance through the entire atmosphere and T_A the effective temperature of the atmosphere. Emissivities and transmittances, as well as the Planck function BB and its inverse TBB are evaluated at 11.5 μm. Surface emissivity has a value close to unity. Cloud emissivity varies with cloud thickness and water phase and content. Most atmospheric attenuation of IR window radiation results from water vapor continuum absorption. Cox and Griffith (1979a) indicate that T^* may differ from the emissivity-corrected value of T_b by up to 12 K for very moist atmospheres. The magnitude of atmospheric attenuation of the background IR window radiation varies with the amount and vertical distribution of absolute humidity, the temperature profile and the slant path through the atmosphere. No attempt is made to derive T_b here, since it does not affect the results. A correction for slant path is applied, however, since each region has a different value of θ. All measured temperatures are normalized to an overhead satellite-viewing zenith angle, $\theta = 0°$, by applying a general theoretical limb-darkening function $\gamma(\theta)$. This normalization yields the corrected temperature

$$T = TBB\{BB(T^*)/\gamma(\theta)\} \quad (2)$$

which is the temperature value used throughout this study. The function used here was derived from the results of radiative transfer calculations for 45 aerosol-free atmospheres and 7 satellite zenith angles for the spectral interval 10.0–12.0 μm. This function is shown in Fig. 1 with the average Nimbus-3 empirical broadband (5.0–30.0 μm) function (Raschke *et al.*, 1973).

Visible (VIS) channel (0.55–0.75 μm) measurements are stored as counts ranging from 0 to 63 with a nominal resolution of about 1 km. To achieve an 8 km resolution, only those VIS data at every eighth pixel element and eighth scan line were retained. Thus, only one of the eight VIS sensors was used. Throughout this paper, "brightness" will refer to the VIS count value of a given scene. The VIS count D is related to the square root of the instrument voltage response V, which is linear with the incident radiant power P, or,

$$V = \frac{D^2}{K}, \quad (3)$$

$$P = G(V - V_0), \quad (4)$$

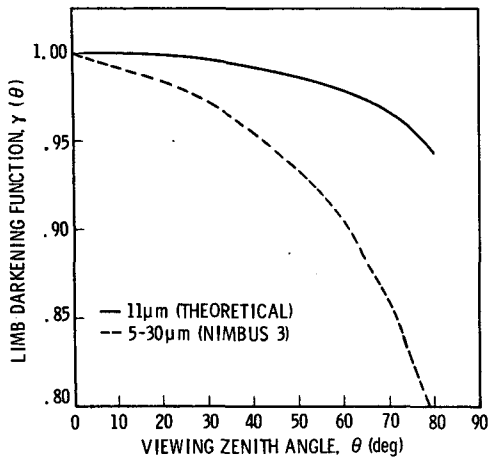

FIG. 1. Limb-darkening models.

where K is a constant, G is the gain, and V_0 the offset voltage. Substituting for V and V_0 in (4) from (3) yields

$$P = G(D^2 - D_0^2)/K, \tag{5}$$

where D_0 is the offset count. Although the VIS channel is not calibrated in terms of absolute radiant power, it is a fairly stable instrument useful for measuring relative brightness.

These data were randomly sampled at the 50% level, and earth-located with a method developed by E. Smith (personal communication, 1978) which has a precision of ±8 km. The data were then associated with one of the 1504 250 × 250 km^2 regions in the grid shown in Fig. 2. This grid represents nearly 20% of the globe and includes two-thirds of the cloud climate categories established by Sherr *et al.* (1968).

3. Methodology for parameter estimations

The methodology for extracting the desired parameters from an hourly VIS–IR data base can be divided into three parts: VIS clear-sky brightness, IR clear-sky temperature and cloud fractions and radiative parameters. The objective of this study is to derive these parameters from the GOES data set itself using a minimum of auxiliary information for the purpose of measuring the effects of clouds on the earth's radiation budget. Accurate retrieval of cloud parameters from such data requires good estimates of the radiative properties of a given scene in the absence of cloud cover since the basic assumption is that the presence of clouds in the sensor field of view alters the clear-sky radiance. Therefore, considerable effort is devoted to the diurnal, geographical and directional variations in the clear-sky radiative parameters. The IR channel is the preferred sensor in this study since the results are needed in a continuous fashion both day and night. However, the VIS brightness for a clear scene is relatively stable and predictable, and usually contrasts well with a cloudy scene. Therefore, it is used to "calibrate" the IR channel hourly during the day to establish a cloud/no-cloud threshold. At night, models are utilized to estimate the IR thresholds using the daytime values as boundary conditions.

Cloud cover is estimated initially from a two-dimensional VIS–IR (day) or one-dimensional IR histogram using an adaptation of the threshold methods of Koffler *et al.* (1973) and Cox and Griffith (1979b). The determination of the IR cloud/no-cloud thresholds by the present technique differs from these earlier methods in that the IR and degraded resolution VIS data are used simultaneously to estimate clear-sky temperature. The threshold is then found by computing the same value of clear-sky temperature from IR data alone. This allows the distribution of the IR data to determine the threshold so that broken clouds may be taken into account. A standard lapse rate of $\Gamma = -6.5$ K km^{-1} is used to approximate the vertical temperature profile. The 24-hour mean clear-sky temperature $\bar{T}_s$ is employed as the lower boundary when applying this lapse rate. Three atmospheric layers are defined by altitude z as

$$\text{lower: } 1, \quad (0 < z \leqslant 2 \text{ km});$$

$$\text{middle: } 2, \quad (2 < z \leqslant 6 \text{ km});$$

and

$$\text{high: } 3, \quad (z > 6 \text{ km}),$$

where $z = (T - \bar{T}_s)/\Gamma$. It is assumed for a given cloudy pixel that the cloud emissivity is unity, the cloud fills the field of view, and the measured temperature corresponds to the physical cloud top. Clouds directly underneath high or middle layer clouds will

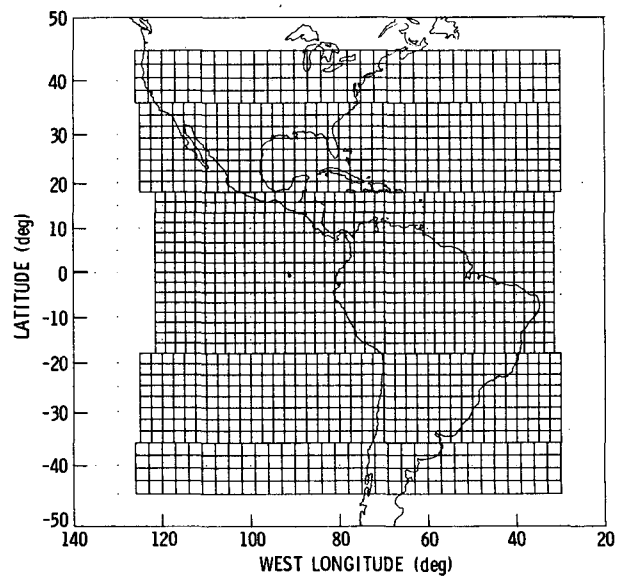

FIG. 2. GOES study regions.

not be detected. After the initial cloud estimate is made, the resultant parameters are checked against certain constraints and adjusted if necessary. Details of this process are described in the following subsections.

a. *Visible clear-sky brightness*

The clear-sky brightness D_s is the mean VIS count associated with the clear portion of a scene. Cloud brightness D_c is the mean VIS count of the cloudy portion of the scene. Total brightness $\bar{D}$ is the mean count of the entire scene.

Clear-sky brightness is determined from models developed with a minimum reflectance technique. A general, visible bidirectional reflectance model was developed from measurements over clear ocean scenes. For each land region, a set of coefficients was derived for use in a simple reflectance model. These models (see Appendix) estimate the clear-sky VIS count for a given set of viewing conditions. The geometry of the viewing conditions is depicted in Fig. 3 where the principal directions are defined by the solar zenith angle ζ, the satellite-viewing zenith angle θ and the viewing azimuth angle ψ, which is measured relative to the solar azimuth.

The clear-sky brightness over water is

$$D_w = \{[\delta_v(\zeta)\chi_v(\zeta, \theta, \psi)\cos\zeta B(0°)/\pi] + D_0^2\}^{1/2}, \quad (6)$$

where δ_v is the visible normalized directional reflectance, χ_v the visible, anisotropic reflectance correction factor and $B(0°)$ the hemispherically integrated brightness count at $\zeta = 0°$. Examples of χ_v for $\zeta = 41.4°$ and $\zeta = 69.5°$ are shown in Fig. 4. It is apparent from this figure that most of the asymmetry in the ocean reflectance patterns is the result of the sunglint phenomenon. Minimum brightness generally occurs for $75° < \psi < 135°$. Some limb brightening is also evident, particularly in the backscattering direction. These results are similar to those found by Raschke and Bandeen (1968).

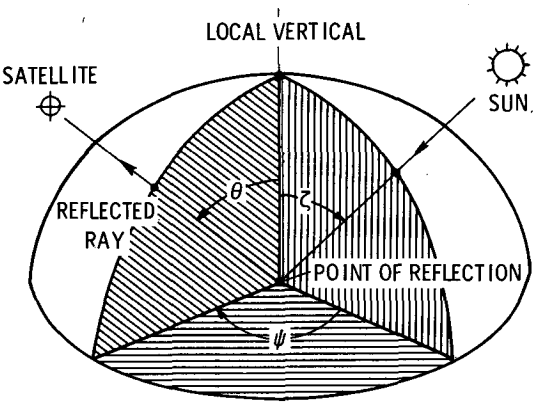

FIG. 3. Angular relationships for Earth radiation measurements.

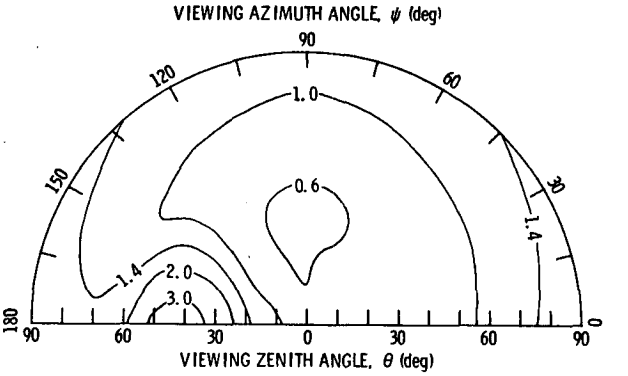

(a) Sun zenith angle = 41.4°

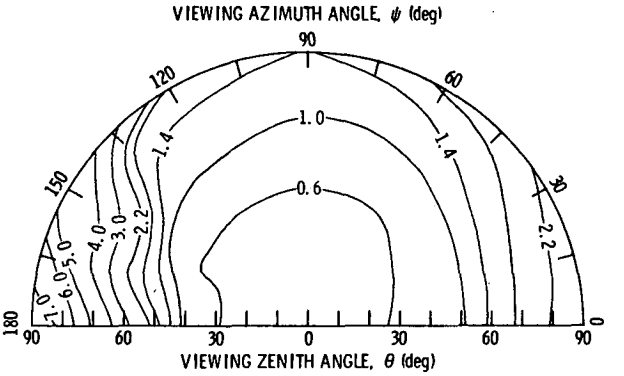

(b) Sun zenith angle = 69.5°

FIG. 4. Ocean visible bidirectional reflectance models.

A model having the form

$$D_g(\phi, \lambda) = a_0 + a_1\cos\zeta + a_2\cos\psi\sin\zeta + a_3\cos^2\psi\sin\zeta \quad (7)$$

(Tarpley, 1979) was employed to estimate the clear-sky brightness D_g over a given land region centered at latitude ϕ and longitude λ. The coefficients

$$a_i = a_i(\phi, \lambda)$$

were found through multiple regression on a set of minimum brightness measurements, $D_{\min}$, for each region using the process described in the Appendix. In almost all regions, the standard errors of the estimated counts ranged from 0.1 to 0.9. Examples of the data fit with this regression model are shown in Fig. 5 for a region in northern Mexico at 30.4°N, 108.8°W. The viewing zenith angle is $\theta = 50.7°$ and the relative azimuth angle ranges from 20° in the morning to 103° in the afternoon. The reflectance anisotropy for this region is significant. For example, the brightness at $\zeta = 63°$ [0848 Local Time (LT) and 1448 LT] varies by more than 100%, from a value of 19^2 in the morning to 13^2 in the afternoon. It was found that maximum reflectance usually occurs in

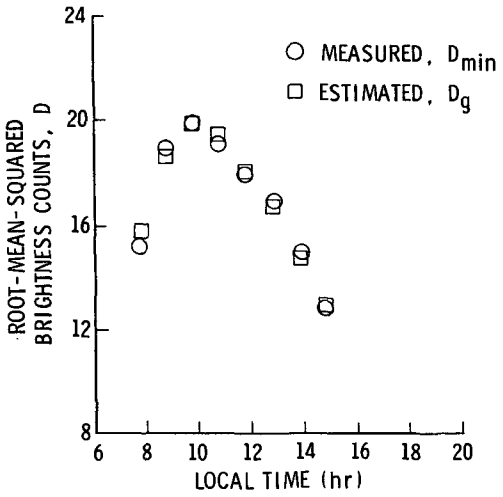

FIG. 5. GOES-observed mean minimum visible brightness counts and modeled estimates for a region in Mexico for November 1978 (latitude = 30.4°N, longitude = 108.8°W).

the backscattering direction, and anisotropy increases with both increasing solar and viewing zenith angles.

For any region, the clear-sky brightness is

$$D_s^2 = D_w^2(\zeta, \theta, \psi)[1 - P(\phi, \lambda)] + D_g^2(\phi, \lambda, \zeta, \psi)P(\phi, \lambda), \quad (8)$$

where $P(\phi, \lambda)$ is the land fraction in the region. In general, the value of D_s is within one count of the original measured minimum brightness. These modeling results indicate that the anisotropy in reflected radiance patterns should be taken into account to avoid diurnally biased estimates of cloud cover and radiative parameters.

Most natural surfaces do not have a constant albedo for a given solar elevation. The albedo of land surfaces, especially bare soils, varies as a function of surface dampness (Idso *et al.*, 1975) or vegetative growth stage (Kondratyev, 1973). Wind speed, turbidity and depth can affect the albedo of water surfaces. While the minimum brightness technique may not always yield the most accurate instantaneous surface–atmosphere reflectance, it is useful for detecting the presence of clouds and may be the best approximation of clear-sky brightness available without the use of auxiliary data.

b. Clear-sky temperature

Clear-sky temperature T_s is the measured or modeled temperature of a cloud-free scene. When both IR and VIS data are available, the clear-sky temperature is estimated with a clear-radiance technique. This approach assumes that there is no cloud contamination in a given measurement T_i, if the colocated VIS count D_i does not exceed a specified threshold D_t. That is,

$$T_s = TBB[\sum_{i=1}^{n_s} BB(T_i)/n_s], \quad (9)$$

where T_i has a colocated VIS count, $D_i \leqslant D_t$, n_s is the number of clear radiance measurements for the region, $D_t = D_w + 2$ for ocean regions and $D_t = D_g + 2$ for land or mixed land and ocean regions. If $\zeta > 82°$ the measured value of T_s is not retained. The addend of 2 roughly corresponds to the standard deviation allowed in the determination of D_s. It also permits some partially cloud-filled pixels to affect T_s when they are present. In those cases, T_s may actually be lower than the true clear-sky temperature. The actual difference between T_s and the true value will depend on the particular cloud type size and spacing and the cloud fraction.

To reduce the probability of cloud contamination in sunglint-affected areas, values of T_s measured over ocean regions are eliminated whenever $D_s > 14$ and

$$\zeta \leqslant 37°, \quad |\zeta - \theta| \leqslant 26° \quad \text{and} \quad \psi \geqslant 90°;$$

$$37° < \zeta \leqslant 46°, \quad |\zeta - \theta| < 28° \quad \text{and} \quad \psi \geqslant 120°;$$

or

$$\zeta > 46°, \quad |\zeta - \theta| \leqslant 30° \quad \text{and} \quad \psi \geqslant 140°.$$

At times when no clear-radiance temperatures are available, another method is needed to estimate T_s for a given region. A diurnal clear-sky temperature model is employed which uses the measured clear-sky temperatures to determine the best estimate of T_s at any time during a 24-hour period. The model, used for land and mixed regions only, is divided into two parts: daytime and nighttime (see Appendix). In the first part, clear-radiance temperatures are used to estimate T_{sr} and T_{ss}, the sunrise and sunset clear-sky temperatures respectively. Nocturnal clear-sky temperatures are estimated using T_{sr} and T_{ss} in the second part of the model.

Missing daytime clear-sky temperatures T_{sr} and T_{ss} are estimated with a segment of a cosine function,

$$T'_s(t) = T_0 + \Delta T \cos k\omega\Delta t, \quad (10)$$

where $\omega = \pi/2H$, $\Delta t = |12 - t|$, H is the half-day length in hours, t is the local time in hours and k has a value of 1 or 2. The two coefficients T_0 and ΔT are found through regression using the clear-radiance temperatures measured for the given time period (see Appendix). Here T_{sr} and T_{ss} are the values of $T'_s(H)$ when the coefficients are determined for the morning and afternoon hours respectively.

Nocturnal land clear-sky temperatures are found with the empirical model,

$$T'_s(t) = b_0 + b_1(\Delta t)^{-3}, \quad (11)$$

where T_{sr} and T_{ss} are used to derive the coefficients b_0 and b_1. When T_{sr} exceeds T_{ss}, simple linear interpolation between T_{ss} and T_{sr} is used instead of

(11). These models predicted hourly temperatures with a relative uncertainty which is less than 2.3 K. Simple linear interpolation or extrapolation between clear-radiance measurements is used to find $T_s'(t)$ for ocean regions in all conditions and over land regions when overcast conditions, missing data or erroneous data preclude the use of (10) and (11). While T_s is not used in overcast conditions, its value is approximated with interpolation to provide a continuous data base. In all cases, the measured and modeled clear-sky temperatures must meet certain conditions before they can be used (see Appendix).

Some results of this modeling procedure are shown in Fig. 6. These examples depict $\bar{T}_s(t)$ for several surface and climate categories. The diurnal variations in clear-sky temperature illustrated here are typical of the regions found in the GOES field of view. Desert areas show the highest diurnal range, while oceanic regions have the lowest diurnal variations.

The diurnal range of T_s is usually greater than the diurnal range of the corresponding surface air temperature T_a. An example of these two temperatures for a region centered at 34.8°N, 111.5°W is given in Fig. 7. The air temperature shown here is the average monthly mean shelter temperature for Flagstaff, Phoenix and Winslow, Arizona. Air temperature varies by only 7.7 K, while T_s changes by 11.6 K on the average. Fritz (1963) found similar differences in the diurnal ranges of the two temperatures over the United States. The lag between T_s and T_a is typical of the time required for the transfer of sensible heat from the surface to the air at shelter level. The difference between T_s and T_a in a given region will depend on the level of atmospheric moisture, wind speed and surface type. When computed from monthly means, this difference will also depend on the number of days with overcast skies. Air temperature can vary diurnally under overcast skies, but the model for T_s varies linearly in those same conditions.

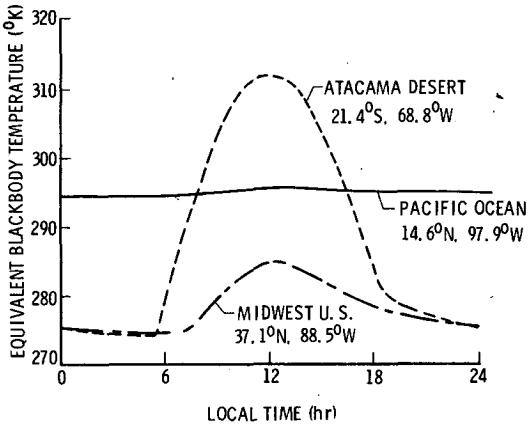

FIG. 6. Monthly mean clear-sky temperatures from GOES for November 1978.

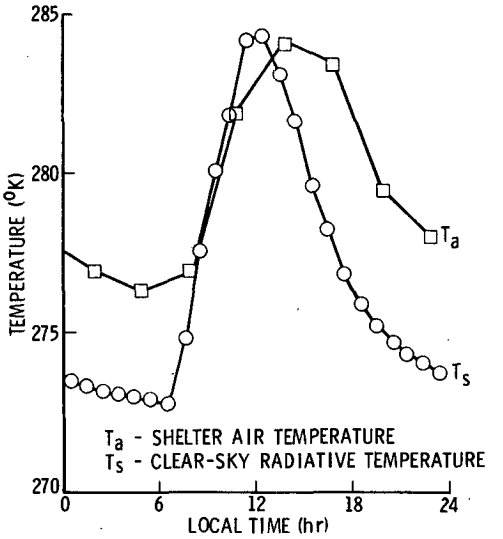

FIG. 7. Shelter air and GOES-observed clear-sky temperatures for November 1978 (latitude = 34.8°N, longitude = 111.5°W).

Clear-sky temperatures derived with the techniques described above are used as a first approximation of the effective clear-sky radiating temperature. These temperatures are used as inputs in the cloud threshold determinations. Final values of T_s will come from the cloud cover algorithm, but, in general, they will not differ significantly from the original estimates.

c. *Infrared threshold cloud estimation procedure*

Cloud amounts and cloud temperatures are found in the following manner for a given value of T_s and an IR histogram. The threshold IR count values k and m corresponding to the temperatures at the bases of layers 2 and 3, respectively, are found from the lapse rate. The base of layer 1 is given by the count j. This count value is computed by progressive summation of count frequencies beginning with the lowest observed count (highest temperature) until the count value j, which satisfies the following inequality, is reached, i.e.,

$$TBB\{\sum_{i=1}^{j} BB(T_i)KNT_i/\sum_{i=1}^{j} KNT_i\} \leqslant T_s,$$

where KNT_i is the number of pixels having the ith count. The fractional clear area is

$$CLR = \sum_{i=1}^{j} KNT_i/n,$$

where n is the total number of pixels. The fraction of cloud cover in the lowest layer is

$$C_1 = \sum_{i=j+1}^{k} KNT_i/n, \qquad (12)$$

and its temperature is

$$T_1 = TBB\{\sum_{i=j+1}^{k} BB(T_i)KNT_i / \sum_{i=j+1}^{k} KNT_i\}. \quad (13)$$

Similarly, the cloud fractions and cloud temperatures in layers 2 and 3 are found with Eqs. (12) and (13) using the appropriate summation limits. Total cloud amount is $C = 1 - CLR$, and the total effective cloud-top temperature is

$$T_c = TBB\{[BB(T_1)C_1 + BB(T_2)C_2 + BB(T_3)C_3]/C\}.$$

If it is assumed that the mean VIS count measured for the region at a given time is

$$\bar{D}^2 = (1 - C)D_s^2 + CD_c^2, \quad (14)$$

then the regional average cloud brightness D_c can be calculated by using the threshold-derived values of C and the value of D_s determined earlier. The use of (14) is a variation on the bispectral method of Reynolds and Vonder Haar (1977) which assumes cloud brightness and solves for cloud amount. In this case, the value of D_c represents the mean cloud brightness of the ensemble of data points and will vary according to the cloud types in the region at the time of measurement.

The basic cloud retrieval scheme is summarized in Fig. 8 which shows a 4 × 8 km resolution, VIS–IR histogram and the corresponding IR and VIS images for a stratocumulus cloud field off the coast of Chile. The numbers on the plot give the frequency of a given IR–VIS pixel pair. The value of D_t is 14 counts based on D_s = 12.2 counts from (8). Clear-sky temperature, T_s = 289.9 K, is computed from the 1347 pixels with $D \leq 14$. It appears that T_s is contaminated by some partially cloud-filled pixels which are not very bright, but are thick enough to reduce the outgoing IR from the surface. The slow response time of the IR sensor may also explain some of these apparently mismatched VIS–IR pairs. To compute this same temperature from the warmest IR pixels according to (11) requires the 2049 pixels with $T > 286.5$ K, the value of T which becomes the IR threshold. This is equivalent to setting the VIS threshold to 18 counts. The total cloud fraction in this case is 0.63 and the mean cloud temperature is 283.0 K.

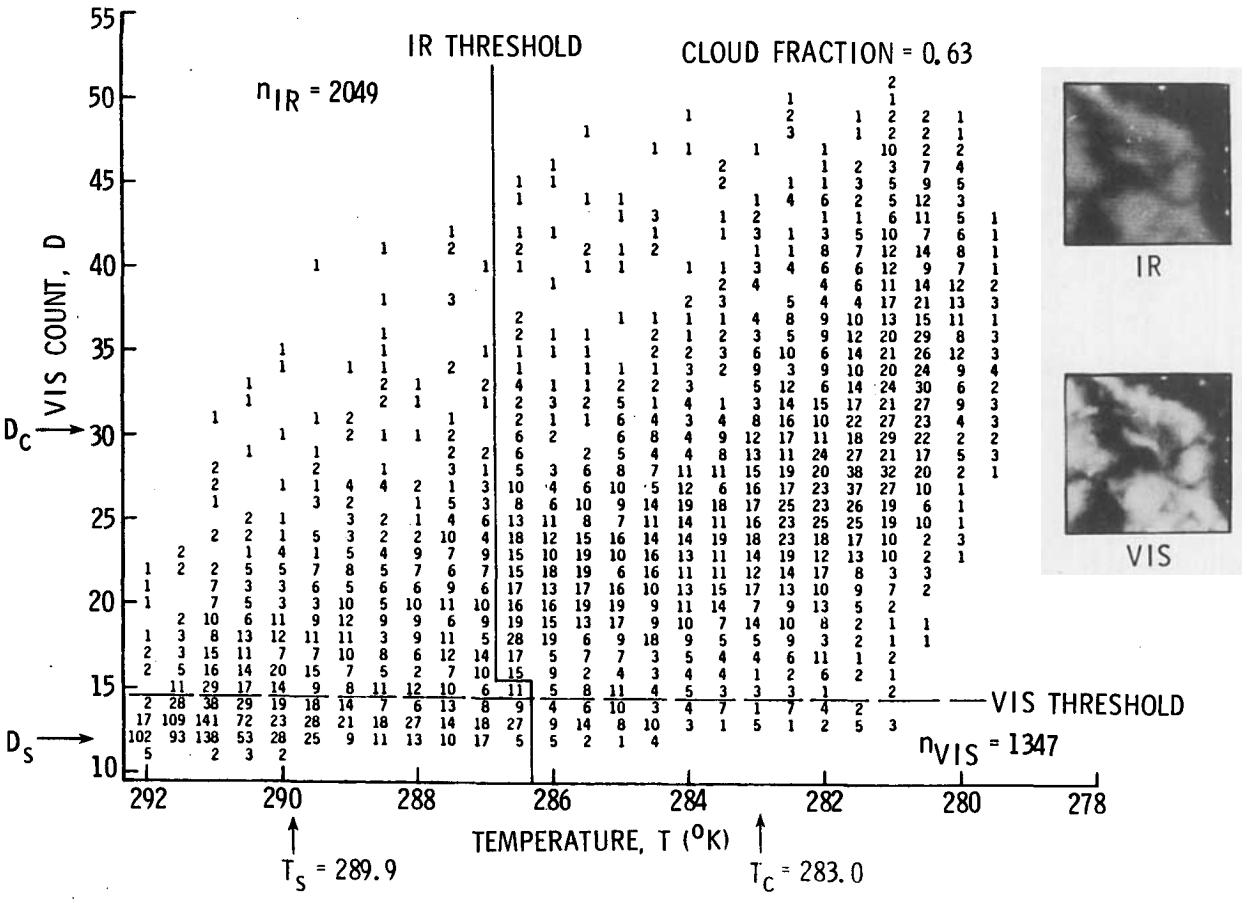

FIG. 8. Example of two-dimensional visible–infrared histogram analyzed with the hybrid bispectral threshold method (4 km resolution).

In this example, only low clouds are present so $C_1 = C$. Using the average VIS count of 25.0 for this scene and the values of D_s and C in (14) yields $D_c = 30.2$.

There are certain situations which require some further processing to minimize errors and avoid unrealistic values. Adjustments in the temperature thresholds are made for bispectral data whenever the total cloud cover is less than a minimum amount. This lower limit is the equivalent amount of optically thick (brightest) cloud cover as determined from the VIS data. Because of the distinct temperature contrast between thick, high- and middle-level clouds and the surface, cloud cover at these levels may usually be determined with relative ease. Low-cloud temperatures may be difficult to distinguish from the clear-sky temperature, especially over land at night. Therefore, several additional constraints are employed to minimize the ambiguities which may arise when low-cloud cover is estimated from unispectral data.

After initial estimates of CLR and C are made, the temperatures T_s and T_1 are differenced to ensure that the result is not less than an allowed minimum temperature difference $\Delta T_{\min}$, derived from the bispectral results. Another correction is made whenever the daily minimum clear-sky temperature is less than $\bar{T}_s - 10$. This occurs most often in desert areas and causes considerable confusion for both low- and middle-cloud estimations. In these situations, T_1 and T_2 are not permitted to exceed the nearest estimates of T_1 and T_2, respectively, made from preceding bispectral data.

The monthly mean diurnal variability of regional cloud cover and its associated radiative characteristics can be determined by applying this methodology to hourly GOES data and averaging each quantity at each local hour over the course of the month. Examples of these monthly mean hourly quantities are given in Fig. 9 for a region straddling the eastern edge of the Andes centered at 21.4°S, 63.8°W. Although each parameter has been evaluated at 24 points on each plot, the data are represented here with continuous lines to enhance the clarity of each feature. Fig. 9a shows the mean total cloud cover $\bar{C}$ and the mean values of reflected brightness $\bar{D}_c$ associated with the cloud cover. The cloud cover is at a minimum shortly before noon and reaches a maximum in the evening about 9 hours later. It appears to be relatively constant all night and diminishes rapidly after sunrise. Cloud brightness is at a maximum around noon and decreases rapidly with increasing solar zenith angle, although cloud reflectance probably increases.

This apparent convective cycle is more evident in Fig. 9b which shows $\bar{T}_s$, $\bar{T}$ and $\bar{T}_c$. All three temperatures reach peak values near noon coincident with low values of $\bar{C}$. Around noon, $\bar{T}_s$ and $\bar{T}$ begin to diverge until the maximum cloud cover occurs. These two quantities then converge until the lowest value of cloud amount is reached. The mean total cloud temperature $\bar{T}_c$ follows a curve which is more parallel to the total measured temperature than $\bar{T}_s$. As cloud cover builds, both $\bar{T}$ and $\bar{T}_c$ decrease, indicating increases in cloud height. Around sunset, $\bar{T}$ and $\bar{T}_c$

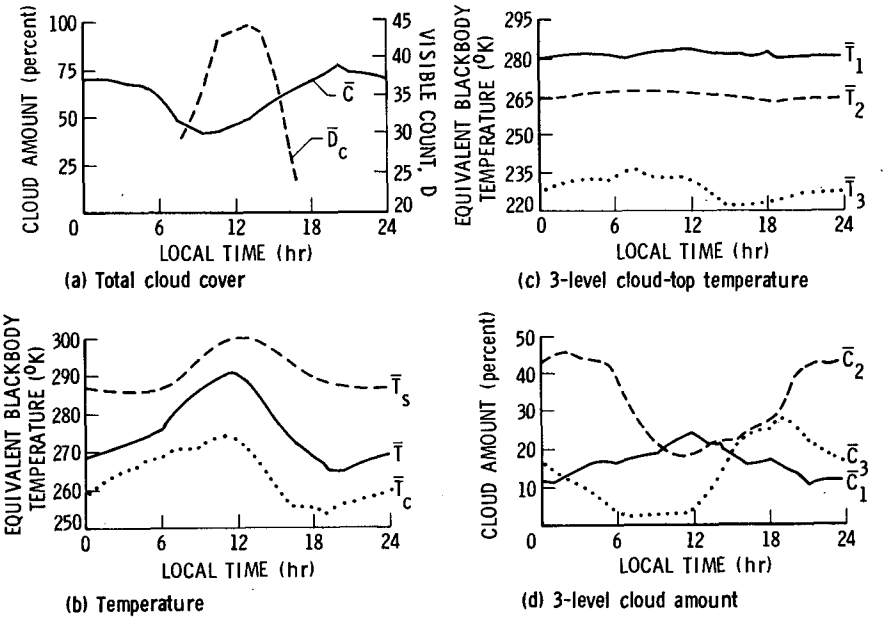

FIG. 9. Monthly mean cloud parameters from GOES for November 1978 (latitude = 21.4°S, longitude = 63.8°W).

begin to increase, but $\bar{C}$ is fairly constant. This may correspond to the dissipation or thinning of a cirrus shield over the main body of clouds. At sunrise, $\bar{T}_c$ begins to flatten and diverge from $\bar{T}$ as the cloudiness decreases and is confined to the lower layers of the atmosphere.

A more detailed view of this is shown in Figs. 9c and 9d. Cloud amounts and cloud temperatures are stratified here. Cloud temperatures in the two lower layers are somewhat constant, although $\bar{T}_2$ is lowest around 1800 LT and both $\bar{T}_1$ and $\bar{T}_2$ reach maximum values around noon when $\bar{C}_1$ is at its peak value and $\bar{C}_2$ is at a minimum. Cloudiness in the upper layers is least extensive and warmest between sunrise and noon. After noon, thick high-altitude clouds build quickly, covering 25% of the region by evening and lowering the cloud-top temperature T_3 by nearly 15 K. The total high-altitude cloud fraction may actually be greater since thin clouds will appear warmer than thicker clouds at the same height. As these apparent cumulonimbus clouds gradually break up, more middle-level clouds or thin, low-emissivity clouds such as cirrus are manifest in the increased values of $\bar{C}_2$. When the middle-level clouds begin to diminish, $\bar{C}_1$ appears to increase.

4. Errors

Certain simplifying assumptions and values of uncertainties have been noted during the development of this methodology, and some comparisons with other empirical results have also been given. An overview of some potential errors and their qualitative implications is presented in this section, and a more quantitative evaluation of relative cloud amount uncertainty is given in the next section.

Estimates of T_s may be biased in certain areas, such as deserts or mountains, where cooling and heating rates may differ significantly from the model predictions. Underestimation of clear-sky brightness can cause overestimation of D_c and of T_s in the daytime if the brighter portion of the region absorbs significantly less solar radiation than the darker areas. Cloud contamination will cause some underestimation of T_s (see Fig. 8). In ocean areas, the nocturnal estimates of T_s should be nearly as accurate as the daylight values since there appears to be only a slight diurnal ocean-surface temperature cycle (see Fig. 6 and the Appendix). Nighttime estimates of T_s over land are highly dependent on the prediction of T_s at sunrise and sunset. Therefore, any bias in either of the latter quantities may yield a bias in low-cloud cover for the entire night. These effects should be diminished with the use of the constraints derived from the bispectral data. Uncertainties in cloud-top temperature and total cloud amount are highly dependent on the accuracy of T_s. Errors should be relatively low for thick, middle- and upper-layer cloud amounts during the day and at night. Low clouds and fog may be mistaken as clear areas at night, but are detectable with bispectral data. Very thin, isolated cirrus clouds may not be detected, especially over bright land, since the VIS brightness and radiating temperatures of areas covered with these clouds may not be significantly different from the cloud-free areas. Although cloud height may be in error in some cases, it should be noted that the determination of total cloud amount and the radiative effects of clouds are the primary concerns of this study.

The basic assumptions of the threshold method may result in large uncertainties in some parameter values. Occasionally, warm, low clouds may overrun a cooler surface such as cold water off a continent, thereby negating the implicit assumption of warmer clear skies. The spatial resolution of the GOES instruments may cause some overestimation of total cloud fraction. Shenk and Salomonson (1972) demonstrated that the average cloud size in a given region can influence the error in the cloud fraction estimated with two types of threshold techniques. In general, they found that the estimated cloud amount tends to increase relative to the true cloud fraction as the ratio of cloud areal size to sensor areal resolution decreases. This tendency, the problem of partially cloud-filled pixels, is addressed to some degree with the present method by allowing D_t to yield an IR clear/cloud threshold which falls between the totally clear and totally cloudy temperatures. In order to see if the present method overestimates C in broken cloud fields, the methodology of Coakley and Bretherton (1982) was applied to 11 region hours of IR data taken over stratocumulus clouds off the coast of Chile. The Coakley and Bretherton (1982) technique was developed to account for the effects of partially cloud-filled pixels for single layer cloud systems such as stratocumulus. The average difference in cloud fractions derived with the two methods was 0.007 with a standard deviation of 0.07 for cloud amounts ranging from 0.12 to 0.97. While these limited comparisons indicate that the partially cloud-filled pixels may be taken into account equivalently with either method (neither method may yield the true, absolute cloud amount), they do not address the problem of small diameter cumulus clouds, which will probably be overestimated whenever the cloud-top temperatures are close to T_s. Comparisons with results from very high resolution sensors (e.g., Landsat) are required to quantify the problem of small cloud effects. Other effects related to the interpretation of satellite data, such as the effect of sensor response time, are discussed by Cox and Griffith (1979a), Davis *et al.* (1979), Clapp (1964) and Stamm and Vonder Haar (1970).

Sampling errors are likely in some areas since data are missing for 17% of the month. At this level, the sampling error would be insignificant if the missing data occurred in a random fashion. However, dropouts

were more frequent at particular hours (e.g., 1100 GMT) and, at certain hours, data gaps occurred for three or four consecutive days. In a few regions, entire synoptic-scale events may have been missed with substantial bias errors in total cloudiness. To partially alleviate this type of bias and to construct a complete hourly data set for other applications, linear interpolation was used to fill in missing hours.

Another type of sampling error may result from the use of the 50% random sampling. To examine this error, a set of full resolution VIS and IR data equivalent to 11 500 region-hours was sampled to obtain an 8 km data set. The data were then sampled at the 50% level to simulate the sampling employed in the present study. The rms differences between D, T and C for the full resolution case and the sampled case are 0.4 counts, 0.4 K and 0.08 respectively. When averaged over 30 days, these differences are negligible. In the case of clouds, it is also not certain which cloud fraction, sampled or full-resolution, is closer to the true value.

The presence of snow may cause some errors in T_s and in cloud cover estimates. Because it is as bright as clouds, snow may be interpreted as clouds, resulting in overestimation of cloud cover. Areas in the United States where snow depths greater than one inch were reported for five days or more during November 1978 are delineated in Fig. 10. Atmospheric haze may also be interpreted as cloud cover since it tends to increase the total brightness in low albedo areas. No attempt is made here to distinguish haze or snow from clouds.

5. Comparisons of total cloud cover

There are several methods which may be used to derive empirical estimates of cloud amount uncertainty. For monthly means, comparisons may be made with subjective observations from the ground or from satellite photographs. While the latter technique tends to miss thin cirrus (Malberg, 1973), the former method tends to overestimate total cloud amount in scattered or broken cloud fields (Hoyt, 1977). In this section, comparisons are made with results from both subjective techniques in order to evaluate the relative uncertainties in total cloud cover.

To compare surface-based cloud observations with the present results, it is necessary to account for the differences in temporal and spatial resolution between the two data sources. If it is assumed that monthly mean surface-based cloud observations $\bar{C}_s$ in a given region are representative of the mean for the entire region, then it is possible to directly compare monthly mean cloud amounts from both techniques. Monthly mean cloud amounts from all first-order land stations within a given GOES-grid region were averaged to obtain a mean regional value of $\bar{C}_s$. These cloud data were taken from monthly summaries of local climatological data published by the Environmental Data and Information Service. Ship observations from London *et al.* (1981) were averaged over 5° latitude by 5° longitude regions. Corresponding GOES results were averaged into these larger regions. All regions included in this comparison are shown in Fig. 10. Both surface data sets contain some notable limita-

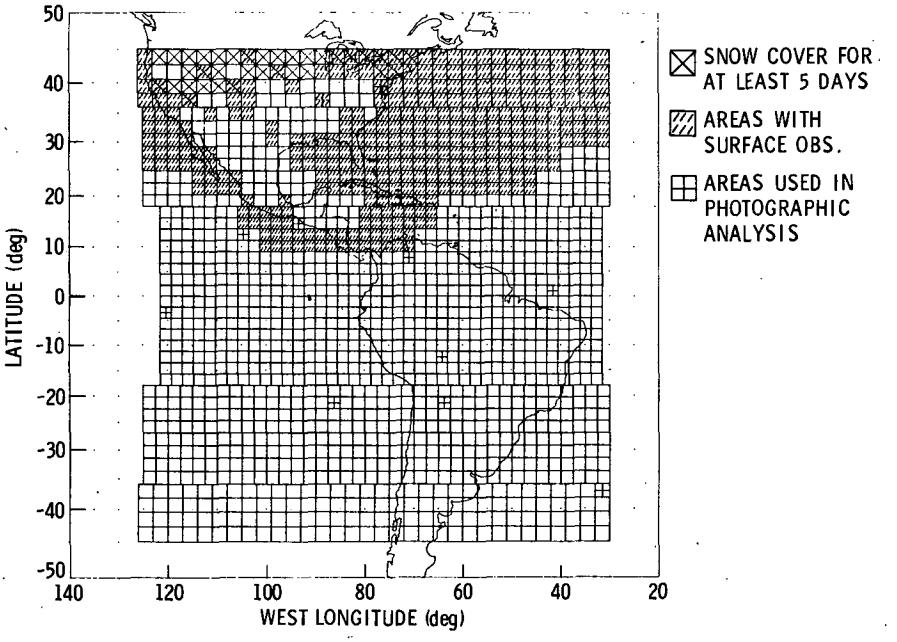

FIG. 10. Snow-covered areas and regions selected for comparing surface observations and GOES photographic analysis results with the HBTM.

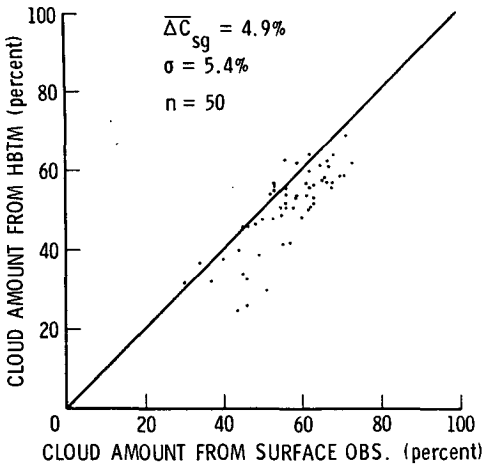

FIG. 11. Correlation of mean cloud amounts from land surface observations and from GOES-East using the HBTM for November 1978. (Line indicates perfect agreement.)

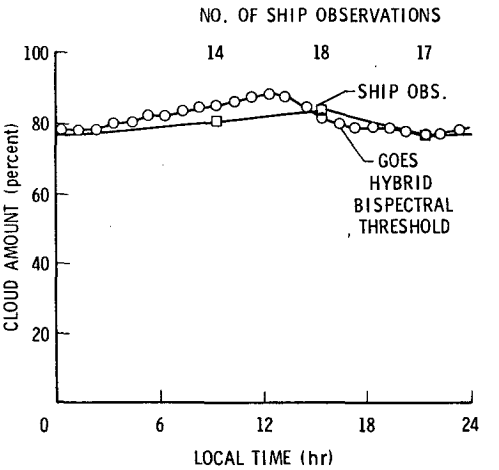

FIG. 13. Comparison of mean cloud amounts from ship observations and from GOES-East using the HBTM for November 1978 (latitude = 40–45°N, longitude = 35 to 40°W).

tions. The number of ground stations in a given region varies from 1 to 7 and may not be distributed very evenly. For example, the stations may all lie on the coast or in valleys in a given area. Ship data may also contain similar local biases if the shipping lane hugs a coastline, passes through the corner of a particular box, or the observations are actually taken from continental or island stations. In addition, the ship data used here include only 1–23 November 1978.

The 50 data pairs for land areas are given in Fig. 11 with the line of perfect agreement. It is apparent that there is a tendency for the ground observations to be greater than the satellite estimates. The mean difference between the land- and satellite-derived cloud amounts is $\overline{\Delta C}_{sg}$ = 0.05 with a standard deviation of $\sigma(\overline{\Delta C}_{sg})$ = 0.05. Fig. 12 shows the results for all ocean regions between 30 and 45°N latitude. For these data, the agreement is quite good with $\overline{\Delta C}_{sg}$ = 0.004 and $\sigma(\overline{\Delta C}_{sg})$ = 0.05 for 41 samples. An example of these results is shown in Fig. 13 for a region between 40 and 45°N and 35 and 40°W at a satellite zenith angle of 63°. The diurnal trends as well as the monthly averages are much the same for both data sets. Between 10 and 30°N the close agreement is not as evident, as seen in Fig. 14. On the average, the ship data in this figure tend to be higher than the satellite estimates by 0.09 with $\sigma(\overline{\Delta C}_{sg})$ = 0.09. Agreement seems to be best at the lower and higher cloud amounts and worst around C_s = 0.50. For both land and ocean measurements, $\overline{\Delta C}_{sg}$ = 0.05 and $\sigma(\overline{\Delta C}_{sg})$ = 0.05.

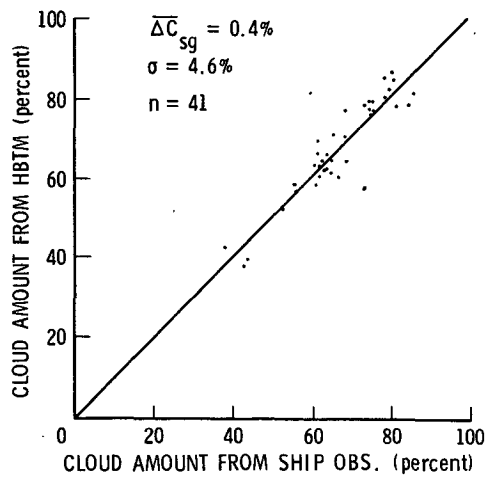

FIG. 12. Correlation of mean cloud amounts from ship observations and from GOES-East using the HBTM for November 1978 (latitude band 30–45°N). (Line indicates perfect agreement).

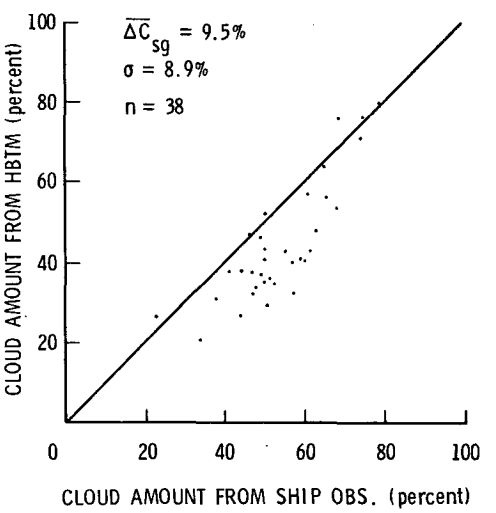

FIG. 14. As in Fig. 12 but for latitude band 10–30°N.

The good agreement over water north of 30°N is probably due to the higher cloud amounts and the types of clouds in this area. Clear and overcast situations with stratiform cloudiness, conditions which are easily quantified, are probably more frequent than broken and scattered cloudiness which is difficult to quantify. South of 30°N, the cloud fraction is lower by about 0.15 and is probably composed primarily of broken or scattered convective clouds (Sherr *et al.*, 1968). Given the findings of Malberg (1973), Hoyt (1977) and Clapp (1964), it is expected that the ground-based observations in areas dominated by broken and scattered cloudiness will be higher by 0.06 to 0.16 than satellite- or aircraft-based, or sunshine-derived values of cloud cover. Some of these differences may also be due to the presence of cirrus clouds which are not thick enough to significantly alter the visible clear-sky radiances and the foreshortening effects which increase with increasing viewing zenith angle.

Differences between all surface observations and GOES results are summarized in Table 1. The greatest bias errors in cloud cover occur when the mean surface-observed cloud cover is between 0.46 and 0.55. These bias errors are about half of those found by Malberg (1973) and Hoyt (1977). One reason for the smaller biases may be the fact that no nighttime data were used in the earlier analyses. A considerable amount of evidence (e.g., Riehl, 1947; Haragan, 1970; Ball *et al.*, 1980) indicates that surface observers underestimate total cloud cover at night relative to their estimates made during the day. Nocturnal surface observations of middle- and upper-level clouds are especially difficult, particularly when there is little moonlight, when haze is present, or when surface lighting is significant.

Visual estimates of cloudiness were also made from GOES imagery for comparisons with cloudiness found with the hybrid bispectral threshold method (HBTM). Although estimates from photographs are also subject to some inherent biases (e.g., Young, 1967), they provide values from the same data set derived in a more conventional manner. Using a torn paper test, Young (1967) was able to show that qualified weather observers with no experience in photographic interpretation or satellite picture analysis tended to overestimate cloud amount from satellite photographs. To overcome this tendency, two satellite analysts familiar with satellite imagery and Young's results were asked to estimate the cloud cover for several regions using GOES-East VIS and IR transparencies for 1400, 1600 and 1800 GMT, and IR images for 0500 GMT taken every second day between 2 and 30 November 1978. The 11 selected regions, shown in Fig. 10, include five oceanic, four land and two coastal regions. The analysts first performed a torn paper test and found results similar to Young (1967). They also found that they tended to overestimate the amount of clear area when it was the desired parameter. Therefore, in the analysis of the GOES images, each analyst estimated both clear and cloudy fractions and reported cloud amount based on a compromise of these two estimates.

The analysts estimated cloud amounts initially from IR and VIS images separately using a four-part grid over each region. In many situations, the analysts noted significant problems in deciding what actually constituted a cloudy or clear situation (possibly due to the presence of thin cirrus, haze, small diameter clouds, or an indistinct infrared background brightness). An attempt was made to eliminate some of the more extreme cases of indecision by having each analyst make second estimates using the IR and VIS infrared photographs together. Each set of readings made by an analyst for a given hour and region was eliminated if the range of cloud amounts exceeded 0.50. To ensure that the data could be compared directly, each sample eliminated from one analyst's data was also removed from the other's data. A total of 571 samples or sets of readings, 91% of the original set, still remained after this process. Averages were computed for each set of readings to yield a single cloud value for each sample.

Differences were computed between the cloud amount estimates made by both analysts and the corresponding values derived with the HBTM. A statistical summary of these differences is shown in Table 2. The mean cloud amount difference $\overline{\Delta C}$ is the average difference in all readings for any two sources. This value plus or minus the standard devia-

TABLE 1. Mean differences ($\overline{\Delta C}_{sg}$) between total cloud fractions from surface observations C_s, and from the hybrid bispectral threshold technique using GOES digital data. Standard deviations are included.

Range of $\bar{C}_s$	$\overline{\Delta C}_{sg}$	σ
0.26–0.35	0.02	0.06
0.36–0.45	0.04	0.06
0.46–0.55	0.07	0.08
0.56–0.65	0.06	0.08
0.66–0.75	0.05	0.07
0.76–0.90	−0.01	0.04

TABLE 2. Mean cloud fraction difference $\overline{\Delta C}$ derived from photographic analysis and the hybrid bispectral threshold method (HBTM) with the standard deviation of: the regional hourly differences σ_1, the mean regional hourly difference σ_2, and the regional mean cloud cover difference σ_3. The rms difference is approximately equal to the value of σ in all cases.

	Analyst I − Analyst II	Analyst I − HBTM	Analyst II − HBTM	Samples
$\overline{\Delta C}$	−0.006	0.003	0.018	571
σ_1	0.08	0.12	0.11	571
σ_2	0.04	0.06	0.04	44
σ_3	0.03	0.04	0.03	11

tion of the hourly difference, σ_1, is the relative uncertainty in a single cloud amount estimate. The relative error in a 15-day mean hourly estimate is represented by $\overline{\Delta C} \pm \sigma_2$, where σ_2 is the standard deviation of the differences in mean regional hourly cloud amounts. The relative uncertainty in the 15-day mean regional cloud amount is $\Delta\overline{C} \pm \sigma_3$, where σ_3 is the standard deviation in the regional mean cloud amount differences. Because the mean differences are close to zero, the root-mean-square difference is approximately equal to the standard deviation in each time-averaging category.

These results indicate that the HBTM yields 15-day regional mean hourly and mean total cloud amounts which are nearly as precise relative to the subjective estimates as the analysts' estimates are to each other. The hourly rms differences are actually low compared to the standard deviations given by Young (1967). This is probably due to the occurrence of some totally clear or overcast conditions in the images. An example of these results is shown in Fig. 15 for a region west of Chile centered at 21.4°S and 86.3°W. The diurnal trends and cloud amounts from all the sources are much the same in this region which is dominated by stratus and stratocumulus clouds.

Some of the larger differences found between the photo analyses and the HBTM were somewhat systematic with respect to region and/or time. Over the tropical land areas, the largest errors occurred when only IR data were available. The two analysts consistently overestimated cloudiness relative to the HBTM at 0500 GMT for areas which are comprised of mixtures of high mountains and low jungles and are dominated by deep convective processes. The analysts noted difficulty distinguishing clear sky from low clouds in these areas at night.

Another area showing a large difference between observers is the region centered near 1.3°N and 40.0°W off the northeastern coast of Brazil. Analyst I estimated daytime cloud amounts which were nearly 0.10 lower than those found by Analyst II and the HBTM. Both analysts noted considerable difficulty in arriving at firm cloud amounts in either channel—only 76% of the daytime samples were retained. The predominant cloud cover, described by the analysts as diffuse and "stringy," could have been thin cirrus, small diameter cumulus streets (difficult to estimate with 8 km data), or a mix of the two types. An average noontime cloud reflectance of ~20% and uncorrected clear-sky/cloud temperature difference, $T_s - T_c$, of 9 K found with the HBTM for this region could characterize thin cirrus (Shenk and Curran, 1973) as well as small cumulus with an occasional occurrence of optically thick clouds.

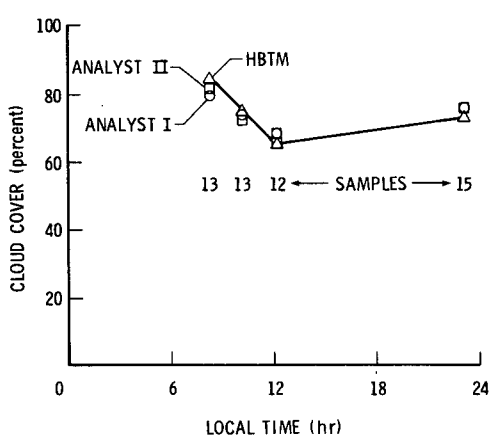

FIG. 15. Comparison of mean cloud amounts from photographic analysis and from GOES-East using the HBTM for November 1978 (latitude = 21.4°S, longitude = 86.3°W).

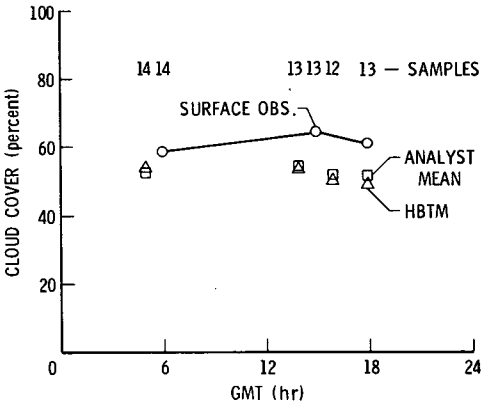

FIG. 16. Comparison of mean cloud amounts from surface observations, photographic analysis and GOES-East using the HBTM for November 1978 for a region in the mideastern United States.

A comparison of all three methods (surface observation, photo analysis and the HBTM) is shown in Fig. 16. The surface observations for the region used in this comparison are the averages of cloud amounts estimated at St. Louis, Missouri; Nashville, Tennessee; and Evansville, Indiana at the days and hours nearest to those in the photo/HBTM comparisons. Differences in average cloud amounts derived by satellite photo analysts and the HBTM are generally small. All of the satellite observations of cloudiness are less than the corresponding surface observations.

6. Summary and concluding remarks

A comprehensive methodology has been developed for deriving hourly regional cloud amounts and cloud radiative parameters from geostationary satellite visible and infrared radiance measurements. This technique, termed the hybrid bispectral threshold method, combines aspects of several previously developed cloud quantification algorithms and improved albedo determinations with an empirical clear-sky temperature

prediction model. Data from GOES-East taken during November 1978 were used to develop the technique and were then analyzed with the HBTM.

Background brightness for each region is determined with a minimum reflectance technique. A general, visible channel bidirectional reflectance model was derived from minimum brightness data over oceans for application to any visible geostationary satellite data. Coefficients for a general land model were determined for each land region but only apply to the November 1978 data set.

Daytime equivalent blackbody clear-sky temperatures T_s are estimated from infrared data corresponding to measured visible clear radiances. Regional cloud cover is estimated on an hourly basis using a threshold method which employs the measured IR histogram, the clear-sky temperature and a fixed lapse rate. Cloud amounts and cloud temperatures are estimated for three altitudes (low, middle and high) by assuming that each pixel corresponds to a homogeneous scene having unit emissivity. The reflected, visible brightness of the cloud-covered portion of the region is then computed from a linear energy balance model which uses the clear-sky VIS count, the average measured VIS count and the infrared-derived cloud amount. Cloud temperature and brightness are then used to adjust the cloud amount whenever certain prespecified limiting conditions are not met.

Objective quantification of cloud cover and related parameters from visible and infrared data on a 24 hour basis over any given scene is a difficult and complex problem. Any quantification scheme, either subjective or objective, suffers from a number of limitations. Some of these limitations have been addressed with the methodology given here. Other aspects may be addressed in future refinement and applications of the present technique. For example, clear-sky brightness may be recomputed from the data for each scene instead of using the prespecified empirical value. Another refinement is the use of cloud brightness to estimate cloud emissivity (if cloud type is known). The relationship between these two quantities is rather imprecise at present, although several studies (e.g., Shenk and Curran, 1973; Reynolds and Vonder Haar, 1977; and Paltridge and Platt, 1981) have produced some encouraging results for cirrus clouds. Clear-sky temperatures may be improved by eliminating much of the cloud contamination left in the present calculations. The present method for estimating clear-sky temperature would be retained for the determination of the IR threshold. Detection of cold, thin cirrus clouds may be accomplished with the use of a limiting, lower-bound, IR threshold independent of the VIS data. Sensitivity checks may be useful in identifying problems with the technique and selecting an alternative approach more suitable for the particular set of conditions. Use of additional auxiliary data, such as snow depth maps, may also eliminate some sources of uncertainty.

The limitations of subjective techniques exacerbate the problem of evaluating the accuracy or comparability of the results of a given objective technique with subjective cloud estimates. Subjective "cloud truth" is fraught with its own set of rather large uncertainties. Nonetheless, most cloud information reported in the past and at present is based on subjective methods. Therefore, it is necessary to know how the cloud cover derived with a given objective method compares with that derived with subjective methods. To provide this sort of evaluation, relative uncertainties in total cloud amounts derived with the hybrid bispectral threshold method were estimated by computing the differences in data derived with two conventional subjective techniques and the HBTM. It was found that monthly average regional cloudiness determined with the HBTM was an average of 0.05 ± 0.05 less than corresponding surface observations taken in many different regions. These results are very similar to earlier comparisons between surface observations and satellite photographic analyses.

Comparisons between photographic analyses and the present technique were also performed. In this case, two satellite data analysts estimated total cloud cover for 11 regions having different climates using 15 days of GOES-East visible and infrared photographs. Root-mean-square in mean regional cloudiness, mean hourly cloud cover and instantaneous cloud amounts derived with the HBTM and from the analysts are 0.04, 0.05 and 0.11 respectively. The corresponding rms differences for the analysts' results relative to each other are 0.03, 0.04 and 0.08. While evaluation of the absolute accuracy of this and other techniques awaits the establishment of an absolute standard, it may be concluded from the results of the above comparisons that both individual and average cloud amounts derived with the hybrid bispectral threshold method are quite reasonable. Further study of the results of this analysis should lead to a better understanding of the diurnal variations of clouds and the radiation budget.

Acknowledgments. The contributions of Messrs. G. G. Gibson, F. M. Denn and J. L. Robbins of Kentron International, Inc. to the analysis and graphical presentation of this data set are gratefully acknowledged. Computer programming support provided by Mr. R. Criste and Ms. G. Lobo of Computer Sciences Corporation has been essential to the execution of this study. The efforts of Ms. J. Cridlin and Ms. B. Johnson in preparing the manuscript are deeply appreciated. We also would like to thank Drs. E. A. Smith and T. H. Vonder Haar of Colorado State University for their assistance in collecting the satellite data for this research.

APPENDIX

Clear-Sky Brightness and Temperature Modeling

1. Ocean clear-sky brightness modeling.

A model to estimate clear-sky brightness for the GOES over water D_w is developed here. This model consists of two parts: a bidirectional reflectance (BDR) model which accounts for the anisotropic reflectance characteristics of water surfaces and a directional reflectance model which estimates the solar zenith angle dependency of visible (VIS) directional reflectance over water. The geometry and angular symbols used here are explained in the main text.

The ocean BDR model was constructed on a basic framework of 84 angular bins for each 0.1 increment of the $\cos\zeta$. These bins were defined by seven 0.1 increments of $\cos\theta$, where $0° < \theta < 72.5°$, and by 12 15° increments of ψ where $0° \leq \psi \leq 180°$, and 180° is the forward scattering direction. Photographs of the November 1978 GOES-2 data were used to select a set of 2.5° × 2.5° oceanic regions which appeared to be relatively cloud free. Histograms of the VIS counts were determined for the selected regions and times. Data representing the minimum 25% were extracted from each histogram. The mean squared brightness, $D^2(\zeta, \theta, \psi)$, and the corresponding standard deviations were computed for each of the extracted subsets. Data having a standard deviation greater than 10% were eliminated. Those values corresponding to the minimum 25% in a given angular bin were used to compute the average brightness for that bin.

This procedure was designed to eliminate cloud contamination and to determine the minimum brightness. Average brightness values were obtained for nearly 45% of the bins. Empty bins, outside of the sunglint area, were filled by interpolating bilinearly between the filled bins unaffected by sunglitter. Those empty bins subject to sunglint were filled using bilinear interpolation with the assumption of symmetry about the specular point.

An additional procedure was used to smooth the model, to facilitate computer processing and to fill the remainder of the hemisphere for $72.5° \leq \theta \leq 90°$. This process used bilinear interpolation to transform the $\cos\theta$ bins to a new bin system which had 10° intervals of θ. Linear extrapolation was used to estimate values at $\theta = 80°$ and $\theta = 90°$. From the aircraft data of Brennan (1969), it appears that linear extrapolation at those viewing angles is a good approximation. The model was developed for solar zenith angles up to 81.4°. Although no water was directly beneath the satellite, some data were obtained at $\zeta = 0°$ for $20° < \theta < 50°$. Average values from the results for $\zeta = 18.2°$ were used to estimate the reflected brightness at other viewing angles for $\zeta = 0°$ after correction for the $\cos\zeta$.

To use these models for other times and data sets, it was necessary to normalize the bin brightness values, $D^2(\zeta, \theta, \psi)$, to the hemispherically integrated brightness,

$$B(\zeta) = \int_0^{2\pi} \int_0^{\pi/2} [D^2(\zeta, \theta, \psi) - D_0^2] \cos\theta \sin\theta d\theta d\psi. \quad \text{(A1)}$$

Equation (A1) was evaluated numerically using the derived bin values. Normalized bidirectional reflectance correction factors

$$\chi_v(\zeta, \theta, \psi) = \pi[D^2(\zeta, \theta, \psi) - D_0^2]/B(\zeta), \quad \text{(A2)}$$

where the subscript v refers to the visible spectrum, were then computed.

The normalized 0.55–0.75 μm directional reflectance,

$$\delta_v(\zeta) = \frac{B(\zeta)}{B(\zeta = 0°)\cos\zeta}, \quad \text{(A3)}$$

was also derived and is shown in Fig. A1 with the averaged normalized data of Raschke and Bandeen (1968).

Application of the clear ocean, visible bidirectional reflectance models derived here requires an estimate of $B(\zeta)$ for an arbitrary value of ζ. The value of $B(0°)$ may be determined from Eq. (A3) using an estimate of $B(\zeta)$ and the value of $\delta_v(\zeta)$ from Fig. A1. Knowing $B(0°)$ and D_0, it is possible to estimate the brightness count D_w for any clear ocean scene with the following equation:

$$D_w = \{[\delta_v(\zeta)\chi_v(\zeta, \theta, \psi)\cos\zeta B(0°)/\pi] + D_0^2\}^{1/2}. \quad \text{(A4)}$$

For the GOES data used here, $B(0°) = 537.0$ and $D_0 = 2.5$.

2. Land clear-sky brightness modeling

Land surfaces also exhibit anisotropic reflectance characteristics. It is not possible to develop a single representative bidirectional reflectance model for land directly from the GOES data since a very limited range of angles is covered. The absolute directional reflectances also may vary considerably from region

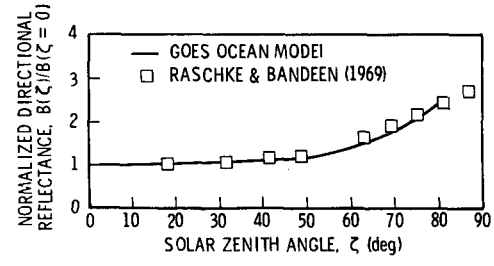

FIG. A1. Visible directional reflectance models.

to region, and the satellite zenith angle is fixed for a given region seen by the GOES. Therefore, the implicit assumption of surface similarity used for the derivation of the ocean model is not applicable to land.

A model having the form

$$D_g(\phi, \lambda) = a_0 + a_1 \cos\zeta + a_2 \cos\psi \sin\zeta + a_3 \cos^2\psi \sin\zeta \quad \text{(A5)}$$

(Tarpley, 1979) was employed to estimate the clear-sky brightness D_g over a given land region centered at latitude ϕ and longitude λ. The coefficients a_0, a_1, a_2 and a_3 were found through multiple regression on a set of minimum brightness measurements for each region using the process described below.

A VIS count histogram was constructed for each region which appeared to be nearly cloud free during several days at the beginning, middle and end of the month. The minimum brightness $D_{\min}$ was determined from each histogram in the following manner:

$$D_{\min} = \left(\sum_{j=1}^{k} \sum_{i=1}^{nj} D_i^2 / \sum_{j=1}^{k} n_j\right)^{1/2},$$

where D_i is the ith measurement in the jth percentile and n_j is the number of measurements in one percentile. The above equation is satisfied when $k > 25$ and the standard deviation of the extracted data or the range of counts exceeds a set of thresholds, or, when $k = 100$. For fairly uniform regions, a range, ΔD, of 8 counts and a standard deviation of $\sigma_D = 1.6$ were allowed. In less homogeneous areas containing a variety of surface features, such as deserts and vegetated mountains, $\Delta D = 10$ and $\sigma_D = 3.2$. No data for $\zeta > 85°$ were used. Only that portion of the region classified as land was observed for the mixed land–water regions. Since it is unlikely that all of the land regions in this study, especially in tropical areas, were completely cloud free for an entire day, it was occasionally necessary to use data from less than 100% of the region.

3. Clear-sky temperature modeling

Clear-sky temperature T_s values are needed at times (e.g., at night) when no clear-radiance temperature can be measured. The model developed here to estimate T_s during these time periods depends on the clear-radiance temperatures measured during the day.

Monthly mean, hourly, bispectral, clear-radiance temperatures defined as

$$\bar{T}_s(t) = TBB\{\sum_{i=1}^{n(t)} BB[T_s(t)_i]/n(t)\},$$

where n is the number of measurements at hour t, were first examined to determine any general trends. Maximum and minimum values of $\bar{T}_s(t)$ were computed for each region. The differences between these two values provides a rough estimate of the regional diurnal variation of T_s. In ocean regions, this variation is typically less than 1.0 K, while in land areas the average daily change in T_s may be as high as 30 K. The time $t_{\max}$ when the maximum value of $\bar{T}_s(t)$ occurred was also determined for each region. These results, given in Table A1, indicate that, on the average, T_s reaches a maximum shortly after local noon for all surface types. The relatively high variance in $t_{\max}$ for oceanic regions is probably due to the low variation in $\bar{T}_s(t)$ and the inclusion of sunglint-affected values. The relatively small lag in the maximum clear-sky temperature with the maximum insolation indicates that, in many cases, the radiating surfaces (vegetation, soil, etc.) respond almost immediately to solar input. For this study, the slight lag of $t_{\max}$ with respect to noon is assumed to be negligible, and the day is divided at noon for modeling purposes.

Clear-sky temperature over land and mixed regions is modeled in three segments (morning, afternoon and night) for each day. The basic approach for estimating T_s utilizes the available clear-radiance data. Values of $T_s(t)$ found in the morning from bispectral data are used to estimate $T_s(t)$ for missing hours in the morning in addition to the sunrise temperature T_{sr}. Similarly, bispectrally-derived, afternoon values of $T_s(t)$ are employed to predict missing afternoon temperatures and T_{ss}, the sunset temperature. Estimates of T_{ss} and of T_{sr} for the following morning are then utilized in a simple linear model to predict surface temperatures during the night.

The prediction models were derived from a selected set of hourly infrared measurements for 14 regions representing several climate regimes. The mean temperature,

$$\bar{T}(t) = TBB\{\sum_{i=1}^{n} BB(T_i)/n\},$$

where n is the total number of pixels in the region, was determined for each region. Clear-radiance temperatures and cloud amounts were also estimated for each hour and region having bispectral data. The bispectral results were then filtered to determine which nights were most likely to be cloud free for a given region. This was accomplished by ensuring that

TABLE A1. Average local time for maximum mean surface (clear-sky) temperature from GOES-East for November 1978.

Surface type	Average time of maximum T (LT)	Standard deviation (h)	Number of regions
Ocean	12.4	2.5	983
Land	12.4	0.8	346
Mixed	12.5	2.1	175

the last cloud cover estimate on a given day and the first cloud estimate on the following day were both less than 10%. If the bispectral data passed this test, and the corresponding unispectral data showed no extreme fluctuations, it was assumed that the intervening night was essentially clear. An example of these data is given in Fig. A2 with the corresponding clear-radiance measurements. Unequal values of T_s and $\bar{T}$ indicate the presence of clouds. Differences between T_s and $\bar{T}$ were substantial when cloud cover exceeded 10%. When cloud amount was less than 10%, the average difference between T_s and $\bar{T}$ was 1.2 K with a standard deviation of 1.7 K. Thus, $\bar{T}$ is a biased estimate of T_s for this selected control data set. To test the model it was assumed that $\bar{T} = T_s$ during times when only unispectral data were available. The resultant values of $T'_s(t)$ were compared to the corresponding values of $T(t)$ to determine which models produced the most precise results.

It was found that the missing daytime clear-sky temperatures and T_{sr} and T_{ss} could usually be determined with a segment of a cosine function,

$$T'_s(t) = T_0 + \Delta T \cos k\omega\Delta t, \qquad \text{(A6)}$$

where $\omega = \pi/2H$, H is the half-day length in hours, $\Delta t = |12 - t|$, t is the local time in hours, and k has a value of 1 or 2. In application, the two coefficients T_0 and ΔT are found through regression using the clear-radiance temperatures measured for the given time period. Regression analysis is then performed for both values of k, and the model having the higher correlation coefficient is used. Separate sets of model coefficients are determined for morning and afternoon because of differences in heating rates for the two time periods.

For nocturnal surface temperatures, it was found that the model

$$T'_s(t) = b_0 + b_1(\Delta t)^{-3}, \qquad \text{(A7)}$$

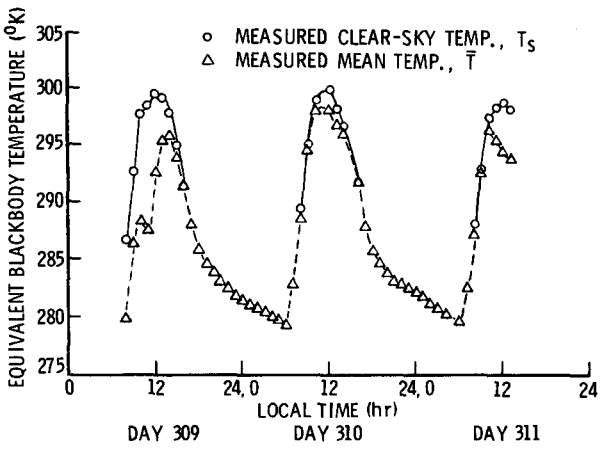

FIG. A2. GOES-measured temperatures (latitude = 28.1°N, longitude = 104.0°W).

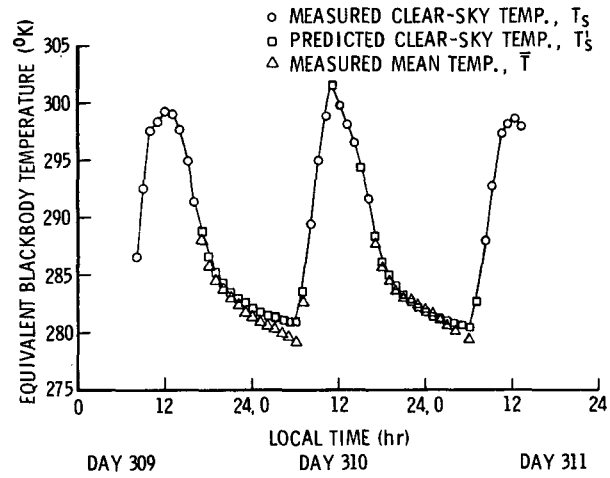

FIG. A3. As in Fig. A2 but for measured and modeled temperatures.

where $\Delta t = t - t_{ss}$, yielded the most precise results. The T_{ss} and T_{sr} found with (A7) were used to derive the coefficients b_0 and b_1. When T_{sr} exceeds T_{ss}, simple linear interpolation is used instead of (A7). The combined daytime and nighttime models produced values of $T'_s(t)$ which differed from $\bar{T}(t)$ by 1.3 K on the average with a standard deviation of 2.3 K. Removal of the bias found in the "control" data set [daytime $T(t)$] yielded a mean error of 0.1 K for T'_s. This modeling is illustrated in Fig. A3. The largest differences here, 1.0 to 1.6 K, occur near sunrise. Cooling rates at night are quite similar for both curves. Overcast conditions, missing data and erroneous data may sometimes preclude the use of (A6) and (A7) over land regions. In all of these cases, simple linear interpolation and extrapolation between clear-radiance measurements are used to find $T'_s(t)$.

Before any values of $T'_s(t)$ are determined with either approach, all clear-radiance data are filtered to remove any gross cloud contamination. Since the visible sensor "sees" only 1/64 of the area viewed by the infrared sensor, it may look at a clear portion of an otherwise cloudy 8 km × 8 km pixel. Therefore, the values of T_s taken from such observations may be more representative of cloudy rather than clear conditions. A similar result may occur when a cloudy pixel is shadowed by a higher or taller neighboring cloud. Thin cirrus clouds may also cause a lower estimate of T_s when their reflectance in the visible spectrum is negligible (Liou, 1974). Removal of all such occurrences in the data is virtually impossible. The more extreme errors may be eliminated with some simple filters.

The first filter removes all temperatures which are less than a limiting minimum T_{min}, which is dependent on surface, location and season. A daytime limit of 260 K was used for areas in the United States. This value was based on air temperature data from

TABLE A2. Constraints on clear-radiance-derived values of surface temperature used to eliminate suspect data for GOES-East, November 1978.

Area	T_{min} (K)	$(\Delta T/\Delta t)_{max}$ (K h^{-1})	ΔT_t (K)	ΔT_d (K)
United States	260	8.0	3.0	30.0
Oceans	273	1.5	0.7	3.0
Central and South America	265	12.0	1.0	45.0
Mixed	265	12.0	3.0	25.0

monthly summaries of local climatological data. While there were times when values less than 260 K did occur, they were infrequent and, in many cases, coincident with snow cover and overcast conditions. A value of 273 K was used for ocean areas. In Central and South America, T_{min} was set to 265 K in order to account for colder mountainous areas.

The second cloud-filtering procedure examines the hourly rate of change in $T_s(t)$. A set of values, $(\Delta T_s/\Delta t)_{max}$, dependent on surface type and location, is established to limit $\Delta T_s/\Delta t$. These are listed in Table A2. They were derived from the monthly means $\bar{T}_s(t)$ and will also vary with season. If the difference between temporally adjacent values of T_s exceeds $(\Delta T_s/\Delta t)_{max}$, the lower value is eliminated. The third cloud filter examines daily trends and checks for unlikely discontinuities in the daily clear-sky temperature curve. In this process, it is assumed that the first, final and maximum clear-sky temperatures measured in a given day are not contaminated. Between $T_s(t_1)$ and $T_s(t_{max})$, $T_s(t)$ is not allowed to decrease from one hour to the next by more than a specified amount ΔT_t, shown in Table A2.

One final limit, ΔT_d was used to constrain the predicted diurnal range of T_s since estimates based on only two or three measurements may occasionally yield unrealistic values. When this limit is exceeded, the value of T_{sr} or T_{ss} is set to the nearest measured value. Linear interpolation is used instead of (A6) whenever $T_{sr} > T_s(12)$ or $T_{ss} > T_s(12)$, and instead of (A7) when $T_{ss} < T_{sr}$. This processing scheme changed or eliminated only 5% of the original clear-radiance estimates.

REFERENCES

Arking, A., 1964: Latitudinal distribution of cloud cover from Tiros III photographs. *Science*, **143**, 569–572.

Ball, J. T., S. J. Thoren and M. A. Atwater, 1980: Cloud-coverage characteristics during phase III of GATE as derived from satellite and ship data. *Mon. Wea. Rev.*, **108**, 1419–1429.

Bean, S. J., and P. N. Somerville, 1981: Some new worldwide cloud-cover models. *J. Appl. Meteor.*, **20**, 223–228.

Brennan, B., 1969: Bidirectional reflectance measurements from an aircraft over natural earth surfaces. NASA TM-X-63564, 82 pp. [NTIS N69-2854].

Clapp, P. F., 1964: Global cloud cover for seasons using TIROS nephanalyses. *Mon. Wea. Rev.*, **92**, 495–507.

Coakley, J. A., Jr., and F. P. Bretherton, 1982: Cloud cover from high-resolution scanner data: Detecting and allowing for partially filled fields of view. *J. Geophys. Res.*, **87**, 4917–4932.

Cox, S. K., and K. T. Griffith, 1979a: Estimates of radiative divergence during Phase III of the GARP Atlantic Tropical Experiment: Part I. Methodology. *J. Atmos. Sci.*, **36**, 576–585.

——, and ——, 1979b: Estimates of radiative divergence during Phase III of the GARP Atlantic Tropical Experiment: Part II. Analysis of Phase III results. *J. Atmos. Sci.*, **36**, 586–601.

Dave, J. V., and N. Braslau, 1975: Effect of cloudiness on the transfer of solar energy through realistic model atmospheres. *J. Appl. Meteor.*, **14**, 388–395.

Davis, J. M., S. K. Cox and T. B. McKee, 1979: Total shortwave radiative characteristics of absorbing finite clouds. *J. Atmos. Sci.*, **36**, 508–518.

Fritz, S., 1963: The diurnal variation of ground temperature as measured from TIROS II. *J. Appl. Meteor.*, **2**, 645–648.

Griggs, M., 1968: Aircraft measurements of albedo and absorption of stratus clouds, and surface albedos. *J. Appl. Meteor.*, **7**, 1012–1017.

Hansen, J., D. Johnson, A. Lacis, S. Lebedeff, P. Lee, D. Kind and G. Russell, 1981: Climate impact of increasing atmospheric carbon dioxide. *Science*, **213**, 957–966.

Haragan, D. R., 1970: An investigation of clouds and precipitation for the Texas high plains. Texas Water Development Board, TDWR/R-111, 128 pp. [NTIS-PB297928].

Herman, G. F., 1980: Thermal radiation in Arctic stratus clouds. *Quart. J. Roy. Meteor. Soc.*, **106**, 771–780.

Hoyt, D. V., 1977: Percent of possible sunshine and the total cloud cover. *Mon. Wea. Rev.*, **105**, 648–652.

Idso, S. B., R. D. Jackson, R. J. Reginato, B. A. Kimball and F. S. Nakayama, 1975: The dependence of bare soil albedo on soil water content. *J. Appl. Meteor.*, **14**, 109–113.

Koffler, R., A. G. DeCotis and P. K. Rao, 1973: A procedure for estimating cloud amount and height from satellite infrared radiation data. *Mon. Wea. Rev.*, **101**, 240–243.

Kondratyev, K. Ya., 1973: *Radiation Characteristics of the Atmosphere and Earth's Surface*, Amerind Publishing, New Delhi, 580 pp.

Kuenning, J. A., T. B. McKee and S. K. Cox, 1978: A laboratory investigation of radiative transfer in cloud fields. Atmos. Sci. Pap. No. 286, Colorado State University, Ft. Collins, 55 pp. [NTIS PB-293018].

Liou, K., 1974: On the radiative properties of cirrus in the window region and their influence on remote sensing of the atmosphere. *J. Atmos. Sci.*, **31**, 522–532.

——, and G. D. Wittman, 1979: Parameterization of the radiative properties of clouds. *J. Atmos. Sci.*, **36**, 1261–1273.

London, J., S. Warren and C. Hahn, 1981: Navy Fleet Numerical Weather Central cloud observations.

Malberg, H., 1973: Comparison of mean cloud cover obtained by satellite photographs and ground-based observations over Europe and the Atlantic. *Mon. Wea. Rev.*, **101**, 893–897.

McKee, T. B., and J. T. Klehr, 1978: Effects of cloud shape on scattered solar radiation. *Mon. Wea. Rev.*, **106**, 399–404.

Miller, D. B., and R. G. Feddes, 1971: *Global Atlas of Relative Cloud Cover 1967–1970 Based on Data From Meteorological Satellites*. Env. Tech. Appl. Ctr., 241 pp. [NTIS N72-22596].

Paltridge, G. W., 1980: Cloud-radiation feedback to climate. *Quart. J. Roy. Meteor. Soc.*, **106**, 895–899.

——, and C. M. R. Platt, 1981: Aircraft measurements of solar and infrared radiation and the microphysics of cirrus clouds. *Quart. J. Roy. Meteor. Soc.*, **107**, 367–380.

Raschke, E., and W. R. Bandeen, 1968: Beobachtungen der Reflexionseigenschaften des Systems Erde-Atmosphare und der Bewolkung uber dem aquatorialen Pazifik von einem synchronen Satelliten aus. *Ann. Meteor.*, **4**, 200–205.

——, T. H. Vonder Haar, M. Pasternak and W. R. Bandeen, 1973: The radiation balance of the Earth-atmosphere system from Nimbus 3 radiation measurements. NASA TN D-7249, 73 pp. [NTIS-N73-2102].

Reynolds, D. W., and T. H. Vonder Haar, 1977: A bispectral method for cloud parameter determination. *Mon. Wea. Rev.*, **105**, 446–457.

Riehl, H., 1947: Diurnal variation of cloudiness over the subtropical Atlantic Ocean. *Bull. Amer. Meteor. Soc.*, **28**, 37–40.

Sadler, J. C., L. Oda and B. J. Kilonsky, 1976: Pacific Ocean cloudiness from satellite observations. UHMET 76-01, 137 pp. [Available from the authors at the University of Hawaii, Honolulu.]

Shenk, W. E., and V. V. Salomonson, 1972: A simulation study exploring the effects of sensor spatial resolution on estimates of cloud cover from satellites. *J. Appl. Meteor.*, **11**, 214–220.

——, and R. J. Curran, 1973: A multispectral method for estimating cirrus cloud top heights. *J. Appl. Meteor.*, **12**, 1213–1216.

Sherr, P. E., A. H. Glaser, J. C. Barnes and J. H. Willand, 1968: World-wide cloud cover distributions for use in computer simulations. NASA CR-61226, 272 pp. [NTIS-N68-32282].

Short, D. A., and J. M. Wallace, 1980: Satellite-inferred morning-to-evening cloudiness changes. *Mon. Wea. Rev.*, **108**, 1160–1169.

Stamm, A. J., and T. H. Vonder Haar, 1970: A study of cloud distributions using reflected radiance measurements from the ATS satellites. *J. Appl. Meteor.*, **9**, 498–507.

Tarpley, J. D., 1979: Estimating incident solar radiation at the surface from geostationary satellite data. *J. Appl. Meteor.*, **18**, 1172–1181.

Vonder Haar, T. H., G. G. Campbell, E. A. Smith, A. Arking, K. Coulson, J. Hickey, F. House, A. Ingersoll, H. Jacobowitz, L. Smith and L. Stowe, 1981: Measurements of the earth radiation budget from satellites during the First GARP Global Experiment. *Adv. Space Res.*, **1**, 285–297.

Young, M. J., 1967: Variability in estimating total cloud cover from satellite pictures. *J. Appl. Meteor.*, **6**, 573–579.